Available online at www.sciencedirect.com
SCIENCE DIRECT®
Journal of Power Sources 143 (2005) 203–211
JOURNAL OF POWER SOURCES
www.elsevier.com/locate/jpowsour

Stable crack growth in nanostructured Li-batteries

K.E. Aifantis [a,*], J.P. Dempsey [b]

[a] *Department of Applied Mathematics and Theoretical Physics, University of Cambridge, UK*
[b] *Department of Civil and Environmental Engineering, Clarkson University, USA*

Received 26 October 2004; accepted 20 November 2004
Available online 18 January 2005

Abstract

The formation of damage, which results from the large volume expansion of the active sites during electrochemical cycling, in rechargeable Li-batteries, is modelled from a fracture mechanics viewpoint to facilitate the selection of the most effective electrode materials and configurations. The present study is a first step towards examining stable cracking in such high-energy storage devices, by considering three different configurations at the nanoscale, which are currently at an experimental stage. As a result, stability diagrams concerning crack growth are constructed and compared for the following cases: (a) the electrodes are thin films, (b) the Li-insertion sites in the anode are nanofibre-like inclusions, (c) the active sites in both electrodes are spherical.

Keywords: Li-batteries; Fracture mechanics; Cracking

1. Introduction

Due to the small Li-intercalation of carbon, which is used as a base material for negative electrodes in rechargeable Li-batteries, extensive research is being performed, for over two decades in order to find alternative anode materials. This research has suggested that some of the best candidates are Sn and Si, due to their high capacity (990 and 4000 mAh g^{-1}). These materials, however, have not been used commercially because of their large volume expansion upon Li-insertion (during the charge/discharge cycle), which results in crumbling and severe cracking of the electrode after continuous electrochemical cycling [15]. It is therefore anticipated that modelling fracture in these high-energy storage devices will provide further insight towards the behavior of these material systems, and allow for the selection of other appropriate materials.

A first attempt to model the mechanical response of Li-batteries, from a purely elastic point of view, during an electrochemical cycle was done by Aifantis and Hackney [1]. The stress-induced inside the electrodes was modelled by treating them as thin films that consisted of disc-shaped Li-ion active sites embedded in an inert glass or ceramic matrix (Fig. 1). This study is a first step towards modelling the most important effect that this cycling deformation process has: cracking. As was shown in experimental evidence provided by Aifantis and Hackney [1] (Fig. 2), continuous electrochemical cycling on a single crystal of $LiMn_2O_4$ resulted in multiple fractures on its surface, producing nanocrystals (Fig. 2). It is believed that continuous cycling would have the same effect on $LiMn_2O_4$ if it were the active site of the cathode; the individual nanoparticles, however, produced by fracture, would no longer be in electrical contact with the remainder of the electrode. As a result the material that fractures loses electrical contact with the electrode and becomes unable to respond to the applied voltage required for charging or controlling the discharge of the battery; hence the electrode becomes unsuitable for further use [1,2].

Moreover, the fracture of individual particles increases the surface area available to chemical attack by the corrosive agents of the battery (HF and residual H_2O) that are believed to attack the surfaces of the active material [1]. In fact, it is reasonable to expect that the chemical instability

* Corresponding author. Tel./fax: +30 2310 995921.
E-mail address: k.aifantis@damtp.cam.ac.uk (K.E. Aifantis).

0378-7753/$ – see front matter © 2004 Elsevier B.V. All rights reserved.
doi:10.1016/j.jpowsour.2004.11.037

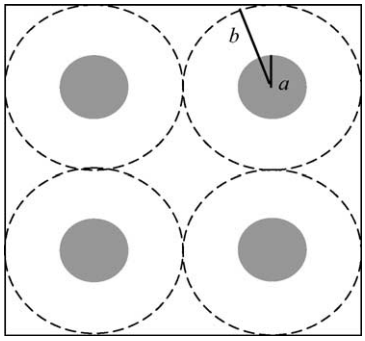

Fig. 1. Idealized geometry of the electrode: Li-insertion particles (shaded) embedded in a glass (blank) matrix. A unit cell is defined by a circle of radius b surrounding a circular particle of radius a.

of the active particle surfaces may interact with the mechanical stress to enhance the structural instability of the material component under consideration (stress corrosion cracking). Many battery developers have taken the approach of using large particle sizes in order to reduce the surface area available to chemical attack. However, this will accentuate the problem associated with stress concentrations at the surface of the particles. An alternative method that can be used is to develop a composite material in which nanoscale electrochemically active material is encased in large particles of a chemically inert matrix [3]. This method not only reduces the surface area of the active material available to chemical attack, but also minimizes the gradients in concentration responsible for fracture, since the active material component of the composite has a nanometre length scale. Therefore, throughout the present work, both electrodes are taken to consist of Li-active sites (with a nanometre diameter) embedded periodically in an inert, with respect to Li, matrix.

Consideration of the above electrode configuration along with fabrication methods that are in the experimental stage allows the mechanical modelling for the following three cases: (a) the active sites are disc-shaped platelets and hence the electrodes take the form of thin films; (b) the active sites of the anode are fibre-like inclusions (long cylinders); (c) the active sites in both the anode and cathode are spherical.

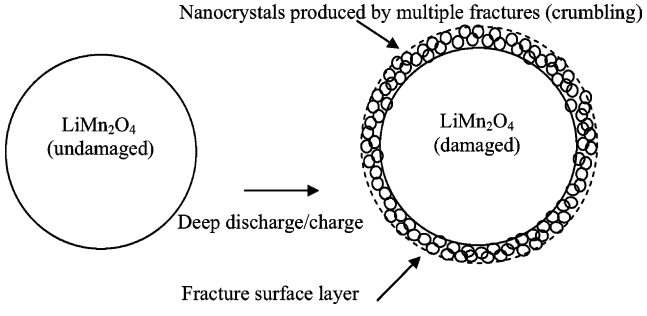

Fig. 2. Schematical representation of fracture zone in a single crystal $LiMn_2O_4$ due to nanocrack formation (damaged surface layer).

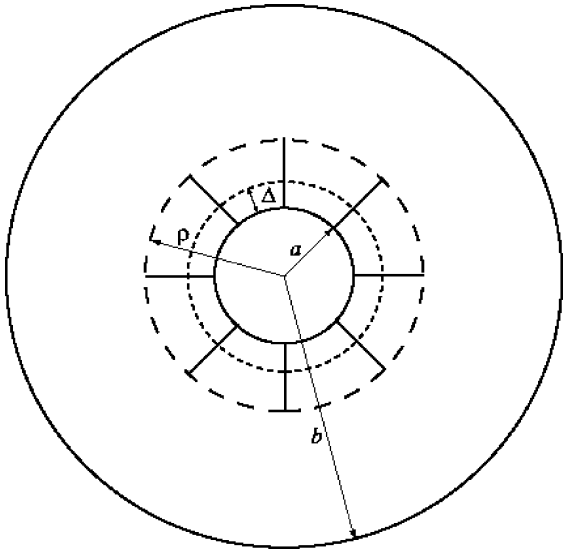

Fig. 3. Radial cracking configuration assumed for the unit cell.

2. Modelling the electrode damage zone

Since experiments [1] have shown that significant damage results from continuous electrochemical cycling it can be assumed that the fracture layer surrounding each active site (Fig. 2) has undergone severe fracture, such that it can support only radial stresses. The damage zone can thus, be modelled by a sufficient number of radial cracks that initiate at the active particle/matrix interface, as shown in Fig. 3. It should be noted that a and b denote the radii of the active Li-insertion site and surrounding matrix, respectively. The pressure the Li-ions induce into the active site is taken to be uniform, and is set equal to p, while the pressure at the outer boundary of the unit cell is taken to be q. It should be noted that this configuration is valid upon maximum Li-insertion, therefore, Δ denotes the maximum expansion of the active sites in the absence of the matrix. Finally, the radii of the radial cracks that form as a result of the continuous charge/discharge cycle are assumed to be equal and their length is $\rho - a$. Since the damage region defined by their length $\rho - a$ may be viewed as supporting only radial stresses (σ_r), all the other stress components vanish ($\sigma_\theta = \sigma_{r\theta} = 0$) inside this zone. This approach is, in fact, similar to that adopted by Dempsey et al. [4] in addressing a similar problem in ice mechanics.

3. Thin film electrodes

In hope of increasing process efficiency and optimizing storage capacity (i.e. Li-intercalation in the negative electrode) significant efforts have been made to prepare anodes that are comprised from thin layers. With this fabrication method it is believed that it will be possible to exceed the electrochemical capacity of bulk anode materials by increasing the amount of Li-insertion sites in the thin film. This has been successfully performed for anodes comprising of tin

composite oxide (TCO) [5] (it should be noted that the active site is the Sn, while the oxide acts as the inert matrix). An additional feature of this configuration is that it contributes to the miniaturization of such devices since the thickness of these films can be 1 nm.

The main advantage, however, from the mechanics point of view, is that this thin film configuration makes it feasible to model the electrodes assuming a state of plane stress; thus, the Li-active sites are treated as disc-shaped platelets, embedded in the inert ceramic or glass matrix. Since the same configuration (and, hence, electromechanical mechanism) may be assumed for both the anode and cathode, the subsequent analysis is valid for both electrodes with the only difference being the Li-insertion site; for example, $LiMn_2O_4$ may be used in the cathode, and Sn in the anode; the matrix will be taken to be soda glass, according to [5].

3.1. General displacement and stress expressions for elasticity in polar coordinates

The stress and displacement expressions in the undamaged active site and matrix can be modelled by using isotropic linear elasticity in polar coordinates. The unit cell under consideration suggests an axially symmetric problem ($\sigma_{r\theta} = 0$); thus, the non-zero stress components and displacements are found by considering the equilibrium relation

$$\frac{\partial \sigma_r}{\partial r} + \frac{1}{r}(\sigma_r - \sigma_\theta) = 0, \tag{1}$$

which in combination with the Airy stress function, Hooke's law and strain compatibility [6] gives

$$\sigma_r = \frac{A}{r^2} + B(1 + 2\log r) + 2C,$$

$$\sigma_\theta = -\frac{A}{r^2} + B(3 + 2\ln r) + 2C, \tag{2}$$

$$u_r = \frac{1}{E}\left[-\frac{A(1+v)}{r} + 2(1-v)Br\log r - B(1+v) + 2C(1-v)r\right], \qquad u_\theta = \frac{4B}{E}r\theta, \tag{3}$$

where (r, θ) denote polar coordinates, (E, v) denote the Young's modulus and Poisson's ratio, and the constants (A, B, C) are to be determined from appropriate boundary conditions.

Since the displacement u_θ should be single-valued, it follows that the constant B vanishes and, thus, the appropriate expressions for the relevant stress and displacement components simplify to

$$\sigma_r = \frac{A}{r^2} + 2C, \qquad \sigma_\theta = -\frac{A}{r^2} + 2C, \tag{4}$$

$$u_r = \frac{1}{E}\left[-\frac{A(1+v)}{r} + 2C(1-v)r\right]. \tag{5}$$

As was mentioned previously, the stress inside the active site is uniform, hence A_s is zero [this also follows from the mathematics, since $A/(0)^2$ is undefined] and Eqs. (4) and (5) reduce to

$$\sigma_r = \sigma_\theta = 2C_s; \tag{6}$$

$$u_r = \frac{2C_s(1-v_s)r}{E_s}, \tag{7}$$

inside the Sn.

3.2. Stress expressions in active site and boundary conditions

According to the discussion, pertaining to Fig. 3, the stresses at the interfaces at $r = a$ and $r = b$ are given by

$$\sigma_r(a) = -p, \qquad \sigma_r(b) = -q. \tag{8}$$

Combination now of Eq. (6) and the first expression in Eq. (8) gives

$$2C_s = -p. \tag{9}$$

Therefore, the stress and displacement expressions inside the active site are given by

$$\sigma_r = \sigma_\theta = -p; \qquad u_r = \frac{-p(1-v_s)r}{E_s}. \tag{10}$$

Since the state under maximum Li-insertion is being examined, the initial stress-free configuration of the active site is taken to be that which it would assume upon reaching its maximum expansion in the absence of any constraints imposed by the surrounding matrix. Since the configuration is radially symmetric, this maximum stress-free volumetric expansion of the Sn corresponds to an increase of its radius, denoted by Δ; therefore, the initial radius of this particle is taken to be $r = a + \Delta$. The surrounding matrix, which is present under the given confined configuration, opposes the aforementioned free expansion by pushing back the active site by a distance δ; therefore, the final radius of the Sn is $r = a + \Delta - \delta$, and the total displacement of the outer surface of the Sn particle at $r = a + \Delta$ is $u_r = -\delta$. Combination of this condition with the second expression in Eq. (10) gives

$$u_r(a + \Delta) = -\delta = -\frac{p(1-v_s)(a+\Delta)}{E_s}. \tag{11}$$

Now the displacement at the active site/matrix interface needs to be formulated. The initial stress-free configuration of the matrix annulus is taken to be that at which no Li-ions have diffused inside the active sites, so the initial inner radius of the glass is $r = a$. As the inner surface of the glass annulus and the outer surface of the Sn particle are in contact, it follows from the above paragraph that once the Sn reaches its maximum expansion Δ, the matrix pushes back a distance δ. Thus, the final inner radius of the glass is $r = a + \Delta - \delta$, and the displacement

condition for the glass at the Sn/glass interface ($r = a$) is $u_r = \Delta - \delta$. Combining this boundary condition with Eq. (11) gives

$$u_r(a) = \Delta - \delta = \Delta - \frac{p(1-v_s)(a+\Delta)}{E_s}. \tag{12}$$

3.3. Stress/displacement expressions in the matrix

The corresponding stress and displacement expressions within the damage region are determined by following an analysis similar to that done by Dempsey et al. [4]. This damage zone is modelled as a system of radial cracks, such that a uniaxial state of stress is assumed to exist within it, i.e. $\sigma_\theta = \sigma_{r\theta} = 0$. Thus, the equilibrium relation given in Eq. (1) reduces to

$$\frac{d\sigma_r}{dr} + \frac{\sigma_r}{r} = 0 \Rightarrow \sigma_r(r) = \frac{k}{r}, \qquad \text{for } a \le r \le \rho, \tag{13}$$

where k is an integration constant. Given that $\sigma_r(a) = -p$, it follows that $k = -pa$. Furthermore, Hooke's law gives

$$\begin{aligned}\sigma_r &= E_g \frac{du_r}{dr} \Rightarrow \frac{du_r}{dr} = \frac{-pa}{E_g r} \Rightarrow u_r(r) \\ &= -\frac{pa}{E_g}\ln(r) + u^*, \qquad \text{for } a \le r \le \rho,\end{aligned} \tag{14}$$

where an expression for the constant u^* can be found by setting the displacement, $u_r(\rho)$, right in front of the crack tip (i.e. just inside the uncracked region) equal to a constant $u_+(\rho)$ and then substituting back into Eq. (14)

$$\begin{aligned}u_r(\rho) &= u_+(\rho) \Rightarrow u_+(\rho) = -\frac{pa}{E_g}\ln(\rho) + u^* \Rightarrow u^* \\ &= \frac{pa}{E_g}\ln(\rho) + u_+(\rho),\end{aligned} \tag{15}$$

then insertion of Eq. (15) in Eq. (14) concludes that inside the cracked region the radial displacement is given by

$$u_r(r) = \frac{pa}{E_g}\ln\left(\frac{\rho}{r}\right) + u_+(\rho), \qquad \text{for } a \le r \le \rho. \tag{16}$$

The uncracked region lies between the crack tip boundary ($r = \rho$) and the glass/glass interface ($r = b$), and it can be treated as a hollow disc that is subject to an internal pressure p_* and an external pressure q (exerted from the neighbouring unit cell). The internal pressure is equal to that present at the interface with the fractured region (i.e. at $r = \rho$) and it can be found by direct substitution in Eq. (13), i.e.

$$p_* = -\sigma_r(\rho) = \frac{pa}{\rho}. \tag{17}$$

The displacement solution for a plane strain configuration (i.e. a hollow cylinder) that is subjected to an internal and external pressure, is given by Westergaard [7]; for the present case, it is modified to plane stress ([8], p. 103), as

$$\begin{aligned}u_+(r) = \frac{r}{2\mu_g}\Bigg\{ & p_* \frac{(b^2/r^2) + ((1-v_g)/(1+v_g))}{(b^2/\rho^2) - 1} \\ & - q\frac{(\rho^2/r^2) + ((1-v_g)/(1+v_g))}{1 - (\rho^2/b^2)}\Bigg\} \\ & \text{for } \rho \le r \le b,\end{aligned} \tag{18}$$

where $\mu_g = E_g/[2(1+v_g)]$ is the shear modulus of the uncracked glass matrix and $u_+(r)$ denotes the corresponding displacement in this region.

Thus, by setting $r = \rho$ in Eq. (18), the following expression for $u_+(\rho)$ is obtained

$$u_+(\rho) = \frac{\rho[b^2(p_* + p_* v_g - 2q) - \rho^2 p_*(v_g - 1)]}{2\mu(v_g + 1)(b^2 - \rho^2)}. \tag{19}$$

Now, insertion of Eq. (19) in Eq. (16) gives a second expression for the displacement at $r = a$

$$u_r(a) = \frac{pa}{E_g}\left\{\ln\left(\frac{\rho}{a}\right) + 2\frac{b^2 - Cb\rho}{b^2 - \rho^2} - (1 - v_g)\right\}, \tag{20}$$

where $C = qb/pa$. The displacement at $r = b$ can also be deduced from Eq. (18) as

$$u_r(b) = \frac{pa}{E_g}\left\{2\frac{b\rho - Cb^2}{b^2 - \rho^2} + C(1 + v_g)\right\}. \tag{21}$$

3.4. Stability index formulation

The question of cracking in rechargeable Li-batteries may now be addressed by considering the hoop stress (σ_θ) just outside the damage zone. This is so because, for the present configuration, σ_θ may be thought of as being the opening tensile stress responsible for crack stability and growth. Using familiar concepts from linear elastic fracture mechanics for radial symmetry [9] the energy release rate, G, can be defined as a function of crack length for this configuration as

$$G(\rho) = \frac{\pi\rho}{E_g n}\sigma_\theta^2(\rho^+), \tag{22}$$

where n is the number of radial cracks, and $\sigma_\theta(\rho^+)$ can be deduced from [4] as

$$\sigma_\theta(\rho^+) = \frac{pa}{b}\left\{\frac{1 + (\rho/b)[(\rho/b) - 2C]}{(\rho/b)[1 - (\rho/b)^2]}\right\}. \tag{23}$$

Now, following [4] the stability index is defined as

$$\kappa = \frac{b}{G}\frac{dG}{d\rho}. \tag{24}$$

It can be seen that the energy release rate depends on the material parameters (E, v), the geometric parameters (a, b), the number of cracks n, as well as on the internal and external pressures p and q. The internal pressure can be found by equating Eqs. (20) and (12) and solving for p, while the

external pressure q need not be defined explicitly as long as C is. Below are solutions for three different outer boundary conditions.

3.5. Three different outer boundary conditions

3.5.1. Case 1: clamped outer boundary

The first case, which is considered, corresponds to the common "manufacturing consistent" configuration according to which the battery system is tightly constrained by the outer casing and, therefore, the displacement at the glass/glass interface is zero. Thus, $u_r(b) = 0$ and in view of Eq. (21), one can solve for C to obtain

$$C = \frac{2b\rho}{(1-\upsilon_g)b^2 + (1+\upsilon_g)\rho^2}. \tag{25}$$

Then inserting Eq. (25) in Eq. (20), and setting the resulting expression equal to Eq. (12), the internal pressure can be explicitly calculated as a function of the geometric and material parameters. Finally, combination of Eq. (22) with Eq. (23) yields the energy release rate for this case, G_1, as

$$G_1(\rho) = \frac{\pi p_1^2 a^2}{nE_g\rho}\left\{\frac{(1-\upsilon_g)b^2 - (1+\upsilon_g)\rho^2}{(1-\upsilon_g)b^2 + (1+\upsilon_g)\rho^2}\right\}^2, \tag{26}$$

where

$$p_1 = \Delta\left\{\frac{a}{E_g}\left[\ln\left(\frac{\rho}{a}\right) + \frac{2(1-\upsilon_g)b^2}{(1-\upsilon_g)b^2 + (1+\upsilon_g)\rho^2} - (1-\upsilon_g)\right] + \frac{(a+\Delta)}{\Gamma}\right\}^{-1}. \tag{27}$$

It should be noted that in Eq. (27), as well as in the expressions to follow, we define $\Gamma = E_s/(1-\upsilon_s)$.

3.5.2. Case 2: traction free outer boundary

The second outer boundary condition was formulated by considering the "natural" condition, according to which the pressure that is induced on the glass by the active site fades with increasing distance and hence the outer pressure (at the glass/glass interface) is zero. Therefore, $q = 0$ (which implies that $C = 0$), and thus, Eqs. (20) and (12) can be used as before to determine the internal pressure, for this case, p_2. Then by using Eqs. (22) and (23) the energy release rate, G_2, is readily calculated as

$$G_2(\rho) = \frac{\pi p_2^2 a^2}{nE_g\rho}\left\{\frac{b^2+\rho^2}{b^2-\rho^2}\right\}^2, \tag{28}$$

where

$$p_2 = \Delta\left\{\frac{a}{E_g}\left[\ln\left(\frac{\rho}{a}\right) + 2\frac{b^2}{b^2-\rho^2} - (1-\upsilon_g)\right] + \frac{(a+\Delta)}{\Gamma}\right\}^{-1}. \tag{29}$$

3.5.3. Case 3: self-equilibrated loading

The final case to be considered is that of "self-equilibrated loading", according to which the force ($2\pi qb$) that is exerted on the glass annulus by the surrounding unit cell is equal to that exerted onto it by the Li-insertion site ($2\pi pa$). Therefore, $C = 1$, and solving for the internal pressure as before, the energy release rate, G_3, for this case is found to be

$$G_3(\rho) = \frac{\pi p_3^2 a^2}{nE_g\rho}\left(\frac{b-\rho}{b+\rho}\right)^2, \tag{30}$$

where

$$p_3 = \Delta\left\{\frac{a}{E_g}\left[\ln\left(\frac{\rho}{a}\right) + 2\frac{b}{b+\rho} - (1-\upsilon_g)\right] + \frac{(a+\Delta)}{\Gamma}\right\}^{-1}. \tag{31}$$

3.6. Stable crack growth in negative electrode

Finally, the stability index, κ, can be computed for each case, via Eq. (24), by letting the radii (a and b) and the material parameters (E_s, E_g, υ_s, υ_g) be (100 and 1000 nm) and (41, 75 GPa, 0.33, 0.25) [10], respectively, while the misfit parameter Δ for these geometric parameters has been found to be 145 nm [1]. (It should be noted that n need not be quantified since κ is independent of the number of radial cracks that form.) Now a stability diagram can be constructed by plotting κ with respect to ρ (Fig. 4). Stable crack growth is examined with the energy release rate G being exactly matched by the resistance to fracture R. An additional necessary condition is that the rate of increase, with change in crack length, of G be less than or equal to the rate of increase of R. Quasibrittle materials require the stability index κ to be negative for stable crack growth; it follows that the more negative the value of κ, the more stable the crack growth becomes, since the difference between final and initial G increases. In this paper, it will be assumed that stable crack growth (slow crack propagation) is feasible only if κ is negative. As the stability index increases, crack growth becomes

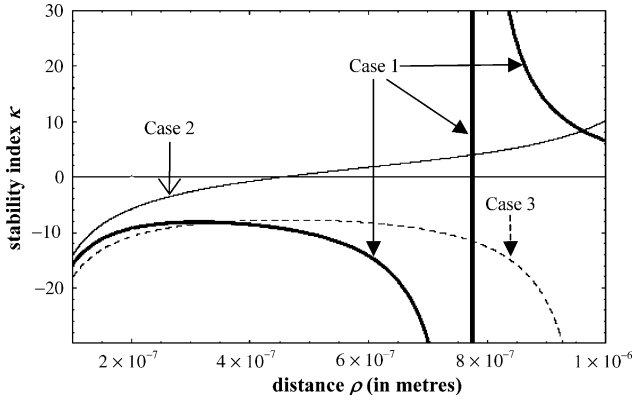

Fig. 4. Stable crack growth in negative electrode for thin film (plane stress) configuration.

more and more unstable. Once the ρ-axis is crossed, unstable crack growth ensues (catastrophic failure is approached very rapidly), hence the ρ-intercept indicates the critical distance to which a crack can propagate stably (the stable critical crack length is found by subtracting the ρ-intercept from the inclusion radius a). It should be noted that in the case that an asymptote is featured in the stability diagram (as in Fig. 4), the crack will close shut well before the asymptote, ρ-axis intercept, is reached. In this case, the energy release rate is decreasing with crack growth; at the asymptote $G = 0$. In particular, it can be seen from Fig. 4 that for Case 2, the corresponding critical stable crack length is rather small, since the ρ-axis is crossed at $\rho = 450$ nm, while for Case 1 ($C > 1$) an asymptote is attained at $\rho = 755$ nm, which implies that the crack will close shut before this distance is reached. Finally, for Case 3, the stability diagram suggests that stable crack growth takes place until the outer radius b.

It can, thus be concluded that the "manufacturing consistent" case is more desirable since the cracks are pinched shut once their critical stable length is approached.

4. Fibre-like active sites

Another fabrication method that is being employed to increase the Li-intercalation in the anode is that according to which the active sites take the form of fibres, whose dimensions are in the sub-micron scale. Experimental observations showed that this method proved to be succesful in the case where the active material was silicon [11] or carbon [12], since this allowed a higher metal content to enter the Li-insertion site. Other anode materials which are still in the experimental stage are Li-capacity templated anodes consisting of about 100 nm SnO_2 nanofibres [1,13].

To analyse the behaviour of the aforementioned anodes, their configuration is taken to be that of long cylindrical active site inclusions embedded in an inert matrix, and thus, conditions of plane strain can be used. The plane stress analysis in Section 3 can be modified for plane strain by making the following substitutions in Eqs. (1)–(31) ([8], p. 103),

$$\left.\begin{aligned} E \to E' &= \tfrac{E}{1-v^2} \\ v \to v' &= \tfrac{v}{1-v} \end{aligned}\right\} \qquad \Gamma \to \Gamma' = \frac{E_s}{(1-2v_s)(1+v_s)}. \tag{32}$$

Therefore, similarly as before a stability diagram can be constructed for this case as shown in Fig. 5. According to [13], the active sites in the anode are taken to be Sn, and the matrix is soda glass.

As in the thin film configuration, Case 2, which corresponds to "natural" conditions allows stable crack growth until a relatively small distance ($\rho = 500$ nm). Under the "manufacturing conditions", Case 1, the crack will close once the stable critical crack distance $\rho = 710$ nm is approached, while the "self-equilibrated loading" case (Case 3), allows for stable cracking until the outer boundary of the unit cell.

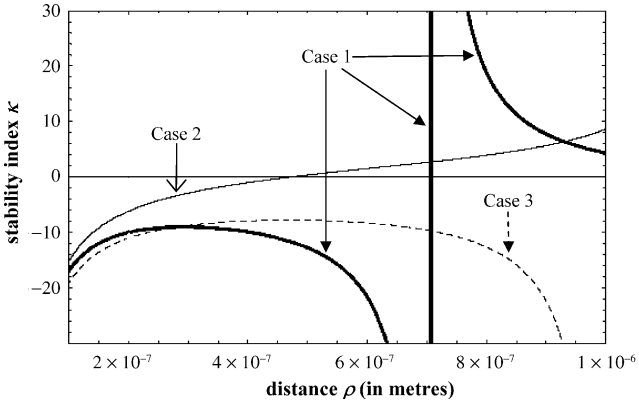

Fig. 5. Stable crack growth in negative electrode with nanofibre-like active inclusions (plane strain).

5. Spherical active sites

As was mentioned in the introduction the third case that shall be examined is that according to which the electrodes are comprised of spherical active sites embedded in a matrix. Studies concerning this electrode configuration are being performed for nanocomposite Sn/C [14], Sn–Fe–C [15] as well as for TCO [1] anodes. In all these systems the Sn acts as the active material.

The quantities considered are the same as in those in Fig. 3, but since we are in three dimensions now the stress and displacement relations change accordingly to

$$\begin{aligned} \sigma_{rr} &= \frac{2C}{r^3} + 2\frac{1+v}{1-2v}D; \\ \sigma_{\theta\theta} = \sigma_{\phi\phi} &= -\frac{C}{r^3} + 2\frac{1+v}{1-2v}D; \\ u_r &= \frac{2(1+v)}{E}\left(-\frac{C}{2r^2} + Dr\right), \end{aligned} \tag{33}$$

while all other stress ($\sigma_{r\phi}$, $\sigma_{r\theta}$, $\sigma_{\phi\theta}$) and displacement (u_θ, u_ϕ) components vanish due to symmetry.

Again, the stress inside the spherical Sn sites does not vary with position and hence $C_s = 0$. Thus, Eq. (33) simplifies to

$$\sigma_{rr} = \sigma_{\theta\theta} = \sigma_{\phi\phi} = 2\frac{1+v_s}{1-2v_s}D_s; \qquad u_r = \frac{2(1+v)r}{E_s}D_s, \tag{34}$$

in the active sites.

Since Eq. (8) still holds, the expressions in Eq. (34) can be re-written in terms of the internal pressure p as

$$\sigma_{rr} = -p \Rightarrow D_s = -\frac{(1-2v_s)}{2(1+v_s)}p \Rightarrow u_r = -\frac{(1-2v_s)rp}{E_s}. \tag{35}$$

The physical reasoning concerning the contraction/expansion of the Sn and surrounding matrix is the same as in Section 3, but in view of the new stress and

displacement expressions established above, Eq. (11) takes the form

$$u_r(a+\Delta) = -\delta = -\frac{(1-2\nu_s)(r+a)p}{E_s}, \tag{36}$$

while the displacement at the Sn–glass interface, Eq. (12), is modified to

$$u_r(a) = \Delta - \delta = \Delta - \frac{(1-2\nu_s)(\Delta+a)p}{E_s}. \tag{37}$$

As was already stated the cracked region supports only radial stresses; hence the force equilibrium relations, under spherical symmetry reduce to

$$\frac{d\sigma_r}{dr} + \frac{2\sigma_r}{r} = 0 \tag{38}$$

solution of which provides the stress inside the damage zone

$$\sigma_{rr}(r) = \frac{k}{r^2}, \qquad \text{for } a \le r \le \rho, \tag{39}$$

where $k = -pa^2$, since the first expression in Eq. (8) implies that $\sigma_{rr}(a) = -p = k/r^2$.

Since the other stress components inside this damage zone vanish, the displacement expression can be determined through the relation of σ_{rr} with u_r as

$$\sigma_{rr}(r) = E_g\frac{du_r}{dr} \Rightarrow \frac{du_r}{dr} = -\frac{pa^2}{E_g r^2} \Rightarrow u_r(r) = \frac{pa^2}{E_g r} + u^*, \tag{40}$$

where the constant u^* is found by continuity of displacements, as in Section 3. Thus, $u_r(\rho)$ is set equal to the displacement right in front of the crack tip $u_+(\rho)$ to give

$$u_+(\rho) = u_r(\rho) = \frac{pa^2}{E_g\rho} + u^* \Rightarrow u^* = u_+(\rho) - \frac{pa^2}{E_g\rho}. \tag{41}$$

It follows that inserting Eq. (41) in Eq. (40) provides the displacement inside the cracked region

$$u_r(r) = \frac{pa^2}{E_g}\left(\frac{1}{r} - \frac{1}{\rho}\right) + u_+(\rho), \qquad \text{for } a \le r \le \rho, \tag{42}$$

while the displacement inside the uncracked glass region (i.e. for a hollow sphere subjected to an internal and external pressure) is given by Westergaard [7] as

$$u_+(r) = \frac{r(1+\nu_g)}{E_g}\left\{p_*\frac{b^3/(2r^3) + (1-2\nu_g)(1+\nu_g)}{b^3/\rho^3 - 1} - q\frac{\rho^3/(2r^3) + (1-2\nu_g)(1+\nu_g)}{1-\rho^3/b^3}\right\}, \quad \rho \le r \le b \tag{43}$$

where p_* is the pressure exerted at $r = \rho$, and is found through Eq. (39) to be

$$p_* = \frac{pa^2}{\rho^2}. \tag{44}$$

Now the displacement right in front of the crack tip can be computed by direct substitution in Eq. (43)

$$u_+(\rho) = \frac{\rho}{2E_g(b^3-\rho^3)}\left\{p_*[(1+\nu_g)b^3 + 2(1-2\nu_g)\rho^3] - q[3b^3(1-\nu_g)]\right\}. \tag{45}$$

Similarly as before a second expression for the displacement at the Sn/glass interface ($r = a$) is obtained by inserting Eq. (45) in Eq. (42)

$$u(a) = \frac{pa^2}{E_g}\left\{\frac{1}{a} - \frac{2(1-\nu_g)}{\rho} + \frac{3(1-\nu_g)(b^3 - Sb\rho^2)}{2\rho(b^3-\rho^3)}\right\}, \tag{46}$$

where $S = qb^2/(pa^2)$. The displacement at the outer glass boundary ($r = b$) is also found through Eq. (43)

$$u(b) = \frac{pa^2}{2bE_g}\left\{\frac{3(1-\nu_g)(b^2\rho - Sb^3)}{b^3-\rho^3} + S(1+\nu_g)\right\}. \tag{47}$$

Finally, Eq. (24) for the stability index is still valid, but in spherical coordinates the energy release rate (according to Dempsey et al. [9]) is defined as

$$G(\rho) = \frac{2(1-\nu_g)\rho\sigma_{\theta\theta}^2(\rho^+)}{nE_g}, \tag{48}$$

where,

$$\sigma_{\theta\theta}(\rho^+) = \frac{pa^2}{b^2}\left[\frac{1 - 3S(\rho/b)^2 + 2(\rho/b)^3}{2(\rho/b)^2(1-(\rho/b)^3)}\right]. \tag{49}$$

5.1. Three different outer boundary conditions

5.1.1. Case 1: clamped outer boundary

Since $u(b) = 0$ in the manufacturing consistent case, Eq. (47) is set equal to zero and S is found to be

$$S = \frac{3(1-\nu_g)b^2\rho}{2(1-2\nu_g)b^3 + (1+\nu_g)\rho^3}. \tag{50}$$

Inserting Eq. (50) in Eq. (46) and then setting the resulting expression equal to Eq. (37), gives the internal pressure, which can in turn be substituted in Eq. (48) to give

$$G_1 = \frac{2(1-\nu_g)a^4p^2}{nE_g\rho^3}\left[\frac{(1-2\nu_g)b^3 - (1+\nu_g)\rho^3}{2(1-2\nu_g)b^3 + (1+\nu_g)\rho^3}\right]^2, \tag{51}$$

where

$$p_1 = \Delta\left\{\frac{a^2}{\rho E_g}\left[\frac{\rho}{a} - 2(1-\nu_g) + \frac{3(1-\nu_g)(1-2\nu_g)b^3}{2(1-2\nu_g)b^3 + (1+\nu_g)\rho^3}\right] + \frac{(a+\Delta)}{\Gamma^{sph}}\right\}^{-1}. \tag{52}$$

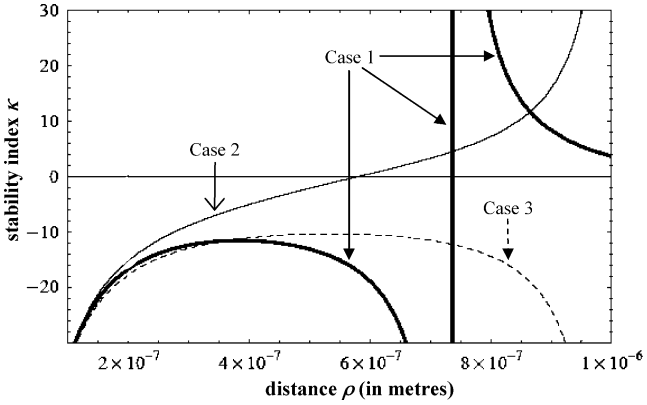

Fig. 6. Stable crack growth in negative electrode with spherical Sn active sites embedded in glass matrix.

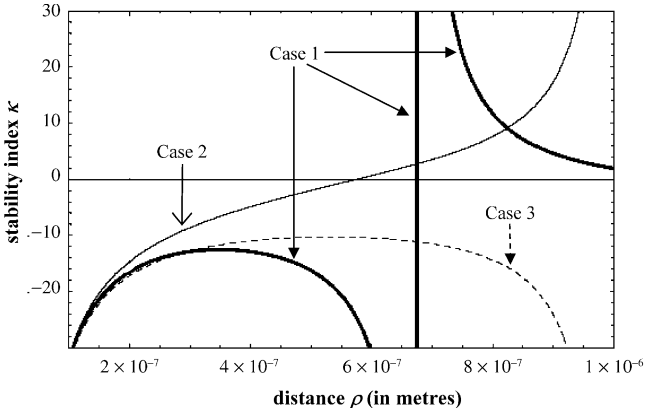

Fig. 7. Stable crack growth in negative electrode with spherical Sn active sites embedded in FeC matrix.

It should be noted that in Eq. (52) as well as in the following relations $\Gamma^{\text{sph}} = E_g/(1-2\nu_g)$.

5.1.2. Case 2: traction free outer boundary

For the traction free boundary condition, $\sigma_{rr}(b) = 0 \Rightarrow q = 0$, hence $S = 0$. Inserting this value of S in Eq. (46) and then setting the resulting expression equal to Eq. (37), G_2 is found as

$$G_2 = \frac{(1-\nu_g)a^4p^2}{2nE_g\rho^3}\left[\frac{b^3+2\rho^3}{b^3-\rho^3}\right]^2, \tag{53}$$

where

$$p_2 = \Delta\left\{\frac{a^2}{\rho E_g}\left[\frac{\rho}{a} - 2(1-\nu_g) + \frac{3(1-\nu_g)b^3}{2(b^3-\rho^3)}\right] + \frac{(a+\Delta)}{\Gamma^{\text{sph}}}\right\}^{-1}. \tag{54}$$

5.1.3. Case 3: self-equilibrating loading

For the case of self-equilibrated loading, i.e. $pa^2 = qb^2$, $S = 1$ and the internal pressure is solved as before to give

$$G_3 = \frac{(1-\nu_g)a^4p^2}{2nE_g\rho^3}\left[\frac{(b+2\rho)(b-\rho)}{b^2+b\rho+\rho^2}\right]^2, \tag{55}$$

where

$$p_3 = \Delta\left\{\frac{a^2}{\rho E_g}\left[\frac{\rho}{a} - \frac{(1-\nu_g)}{2} - \frac{3(1-\nu_g)\rho^2}{2(b^2+b\rho+\rho^2)}\right] + \frac{(a+\Delta)}{\Gamma^{\text{sph}}}\right\}^{-1}. \tag{56}$$

The stability diagrams for all cases considered are shown in Fig. 6 (the active sites are again taken to be Sn, according to [14,15], while the matrix is taken to be soda glass for consistency with the previous cases). It can be seen that Cases 1, 2 and 3 allow for critical stable crack growth until $\rho = 737$ nm, 560 nm and 1000 nm, respectively.

Since Sn–Fe–C composites are also under consideration, it is of interest, to examine crack growth when the matrix is FeC, as [15] suggests; hence Fig. 7 is obtained ($\rho = 680$ nm, 600 nm and 1000 nm for Cases 1, 2 and 3).

6. Conclusions

The present study is a first attempt to predict the extent of stable crack growth in Li-ion battery electrodes that comprise of active/inactive nanocomposites. In particular, stability diagrams are obtained for anodes that consist of Tin Composite Oxide, since various nano-configurations (thin film electrodes, fibre-like active sites in anode, spherical active sites) still in the experimental stage employ this material. As can be seen from Figs. 4–7, all configurations examined herein exhibit similar stability behaviour when subjected to the particular boundary conditions considered. For the "manufacturing consistent" case it is desirable to have small critical stable crack lengths, since the stability diagrams suggest that the smaller the critical length, the smaller the distance the crack will propagate before being pinched shut; it should be emphasized that this case is the most desirable since the cracks cannot propagate beyond a certain distance. The "natural" boundary condition, on the other hand, is the least desirable since it is inherently unstable. Finally, no instability was encountered for the "self-equilibrated loading" case; the crack could propagate stably toward the outer boundary of the unit cell.

It follows from the above discussion that the most desirable configuration of all those considered is that of spherical Sn sites embedded in a FeC matrix, having not only the smallest critical stable crack length for the "manufacturing consistent" case, but also the largest critical stable length for the "natural" boundary condition.

A direct extension of the present work is to apply this analysis to other material systems, such as those which use Si as the active site. Moreover, it should be emphasized that the current analysis can allow for the determination of the

critical crack length (ρ_c) at which fracture of the electrode will take place (by substituting the critical energy release rate of the matrix in Eqs. (22) or (48) and solving for ρ_c); additional information can thus be obtained as to which materials, configurations and outer boundary conditions are more appropriate. It may be possible, for example, that the "natural" outer boundary condition can allow for greater critical crack lengths (which do not exceed the critical stable crack length) than the "manufacturing consistent" condition.

For this, however, to be examined the critical energy release rate for soda glass, FeC and other inert ceramics needs to be determined through experiments, since such information is lacking.

Acknowledgements

KEA is grateful to her advisor Professor John Willis for his encouragement and helpful remarks and to the National Science Foundation for its support through its Graduate Research Fellowship Program. Both authors would like to thank Professors Andrew Palmer and Stephen Hackney for their helpful discussions. J.P.D. would like to acknowledge the support of the US Army (by Grant DAAD 19-00-1-0479) and the National Science Foundation (by the OPP Grant 0338226).

References

[1] K.E. Aifantis, S.A. Hackney, J. Mech. Behav. Mater. 14 (2003) 413.
[2] Y. Shao-Horn, S.A. Hackney, A.R. Armstrong, P.G. Bruce, C.S. Johnson, M.M. Thackeray, J. Electrochem. Soc. 146 (1999) 2404.
[3] O. Mao, R.L. Turner, I.A. Courtney, B.D. Fredericksen, M.I. Buckett, L.J. Krause, J.R. Dahn, Electrochem. Solid State Lett. 2 (1999) 3.
[4] J.P. Dempsey, A.C. Palmer, D.S. Sodhi, Eng. Fract. Mech. 68 (2001) 1961.
[5] G. Taillades, J. Sarradin, J. Power Sour. 125 (2) (2004) 199.
[6] A.P. Boresi, K.P. Chong, Elasticity in Engineering Mechanics, second ed., John Willey & Sons, New York, 2000, Chapter 6.
[7] H.M. Westergaard, Theory of Elasticity and Plasticity, Harvard University Press, 1953.
[8] A.C. Ugural, S.K. Fenster, Advanced Strength and Applied Elasticity, third ed., Prentice Hall, New Jersey, 1994.
[9] J.P. Dempsey, L.I. Slepyan, I.I. Shekhtman, Int. J. Fract. 73 (1995) 223.
[10] W.D. Callister Jr., Materials Science and Engineering: An Introduction, sixth ed., John Willey & Sons, 2002.
[11] M. Green, E. Fielder, B. Scrosati, M. Wachtler, J. Serra Morenob, Electrochem. Solid State Lett. 6 (5) (2003) A75.
[12] P. Thomas, D. Billaud, Electrochim. Acta 46 (22) (2001) 3359.
[13] M.M. Thackeray, C.S. Johnson, A.J. Kahaian, K.D. Kepler, J.T. Vaughey, Y. Shao-Horn, S.A. Hackney, ITE Battery Lett. 1 (1999) 26.
[14] I.-S. Kim, G.E. Blomgren, P.N. Kumtaa, Electrochem. Solid State Lett. 7 (3) (2004) A44.
[15] O. Mao, J.R. Dahn, J. Electrochem. Soc. 146 (1999) 405.